Available online at www.sciencedirect.com

jmr&t Journal of Materials Research and Technology

journal homepage: www.elsevier.com/locate/jmrt

Original Article

Graphene wrapped Y_2O_3 coated $LiNi_{0.5}Mn_{1.5}O_4$ quasi-spheres as novel cathode materials for lithium-ion batteries

Hanan Abdurehman Tariq [a], *Jeffin James Abraham* [a], *Aisha Abdul Quddus* [a], *Siham AlQaradawi* [b], *Ramazan Kahraman* [c,**], *R.A. Shakoor* [a,*]

[a] *Center for Advanced Materials (CAM), Qatar University, P. O. Box 2713, Doha, Qatar*

[b] *Department of Chemistry & Earth Sciences, College of Arts and Science, Qatar University, P. O. Box 2713, Doha, Qatar*

[c] *Department of Chemical Engineering, College of Engineering, Qatar University, P. O. Box 2713, Doha, Qatar*

ARTICLE INFO

Article history:
Received 18 November 2020
Accepted 9 July 2021
Available online 19 July 2021

Keywords:
Lithium nickel manganese oxide
Graphene oxide
Chemical co-precipitation
Cathode
Charge/discharge capacity
Rate capability
Energy density

ABSTRACT

$LiNi_{0.5}Mn_{1.5}O_4$ with a high-voltage spinel structure is a potential cathode material for high-energy lithium-ion batteries (LIBs). Y_2O_3 coated quasi-spheres of $LiNi_{0.5}Mn_{1.5}O_4$ covered in graphene (LNMO-YO-G) have been synthesized by a microwave-assisted chemical co-precipitation technique. The coating of quasi-spheres with Y_2O_3 and subsequent wrapping in graphene nanosheets does not modify the bulk structure and inhibits the production of undesirable phases. Thermal analysis indicates that the developed materials demonstrate good thermal stability. The material exhibits an initial capacity of 133 mAh g^{-1} at the C/10 rate with a capacity retention of 98% after 100 cycles. Remarkably, a discharge capacity of 115 mAh g^{-1} is achieved in LNMO-YO-G at a 10C rate, reflecting its extraordinary improvement in the rate capability. Furthermore, after 20 cycles at higher temperature (55 °C), the cathode samples exhibit an excellent capacity of 132 mAh g^{-1}. Y_2O_3 coating reduces the leaching of ions from the electrode, but such coatings reduce the electrical conductivity. Conversely, graphene increases the electrical conductivity, wraps the active particles along an electrically conductive path, and prevents agglomeration. Parasitic reactions are inhibited without compromising electrical conductivity due to the synergistic material design and fast microwave synthesis method. The proposed material synthesis strategy can be effectively extended to other classes of electrode materials to improve their cyclic performance.

* Corresponding author.
** Corresponding author.
E-mail addresses: ramazank@qu.edu.qa (R. Kahraman), shakoor@qu.edu.qa (R.A. Shakoor).

https://doi.org/10.1016/j.jmrt.2021.07.038

1. Introduction

Energy science and storage have been one of the most extensively investigated areas by the research community. The energy cache is perhaps the only factor that can constrain the development of society. The limited supply of fossil fuels that take millions of years to form is depleting much faster than the new sources are created or discovered. Society's sustainability relies on the supply of electricity and the evolution of systems capable of holding clean energy as a primary and secondary source [1–3].

The electrode materials for secondary batteries must comply with the strict battery requirements, such as suitable for intercalation reactions, appropriate electronic and ionic conduction, presence of intercalation sites in the crystal structure, good redox potential, thermodynamic stability, low cost, pronounced safety, and toxicity [4]. The compounds capable of having the properties mentioned above are classified as intercalating materials. Intercalating materials are further classified into three classes, i.e., one-dimensional (olivine structures)-1D, two-dimensional (layered)-2D, and three-dimensional (spinel)-3D. The preferential intercalation sites in these compounds have minimal energy and permit the free flow of ions through the crystal lattice. The availability of new sites and mechanisms changes the materials' power performance, even those previously not considered commercially viable [5].

$LiNi_{0.5}Mn_{1.5}O_4$ is one of the most promising electrodes for energy storage devices due to its high energy density, excellent electrochemical performance, and low environmental impact. However, the capacity fading with the progression of charge–discharge cycles, especially at higher temperatures and voltage ranges, limits the large-scale applications. Moreover, their safety concerns also limit adaption in demanding applications. The discharge capacity decline in $LiNi_{0.5}Mn_{1.5}O_4$ is linked to the undesirable parasitic reactions and degradation of the electrode, particularly at higher temperatures. The Mn^{3+} ions dissolution caused by the Jahn Teller effect degrades electrodes [6]. Moreover, the Mn^{2+} ions tend to dissolve into the electrolyte and accumulate further on the anode surface. Consequently, the accumulation raises the cell impedance, causing the capacity to decay [7,8]. Over the years, there have been many reported methods to modify and tune the intrinsic reaction sites available for intercalation/de-intercalation in the host structures [9]. The electrode's durability can be successfully increased at higher voltages by developing improved electrolytes or coating the bare particles with protective coatings [10].

Many studies have shown ways to minimize direct contact with appropriate coatings between the LNMO electrode and the electrolyte [11–13]. Several research groups have identified numerous coating materials, including oxides [14–16], ionic conductors [17,18], polymers [19], and conductive carbons [20]. These coatings eliminate secondary reactions between the electrolyte and the electrode and improve the electrochemical performance of the cell. Ceramic coatings, for example, are inexpensive and have shown promising results in improving the performance of cathode materials under difficult operational conditions. Ceramic coating reduces the leaching of ions from the electrode, but such coatings also reduce the electrical conductivity. Also, the bulk of these covering materials are electrochemically inactive, resulting in composite materials with low-rate performance [21]. Smart strategies may significantly improve electrochemical efficiency without sacrificing capacity [22,23].

Rare-earth element oxides have higher electrochemical performance and better electrical stability to the host ionic species, making the movement of electrical and ionic species more efficient. It is reported that Y_2O_3 is a viable coating material, and $LiCo_{1/3}Ni_{1/3}Mn_{1/3}O_2$ coated with Y_2O_3 exhibited excellent electrical efficiency as a cathode [24]. The remarkable electrochemical properties, stable chemical characteristics, and large specific surface area of graphene and its compounds have been researched extensively. The synthesis process has a profound impact on microstructures and crystal structures, which have significant impact on the electrochemical performance of cathode materials. Microwave heating is an effective technique for the preparation of $LiNi_{0.5}Mn_{1.5}O_4$ and can reduce time and energy costs. The development of some other cathode materials ($LiMn_2O_4$, Li_2FeSiO_4, $LiFePO_4$) using microwave-assisted techniques has been reported [25–28]. Microwave irradiations play an essential part in grain growth during microwave-assisted reactions. During the heat treatment step, where microwave heating is concurrently applied, microwave irradiation improves crystal lattice structure and enhances cathode materials' capacity [29]. It may also be inferred that microwave heating promotes the development of spinel cathode materials.

In this study, using the established technology of metal oxide, graphene hybrid coatings, and microwave heating, a novel strategy is proposed to synthesize yttria (Y_2O_3) coated $LiNi_{0.5}Mn_{1.5}O_4$ quasi-spheres covered in graphene. First, microwaves are used with chemical precipitation to produce the required cathode material, $LiNi_{0.5}Mn_{1.5}O_4$. Next, the quasi-spheres of $LiNi_{0.5}Mn_{1.5}O_4$ are coated with yttria (Y_2O_3) using the advantageous chemical precipitation method following their wrapping in graphene. The physicochemical, structural, and electrochemical properties of pristine $LiNi_{0.5}Mn_{1.5}O_4$ (LNMO-P), Y_2O_3 coated $LiNi_{0.5}Mn_{1.5}O_4$ (LNMO-YO), and (Y_2O_3) coated $LiNi_{0.5}Mn_{1.5}O_4$ quasi-spheres covered in graphene were investigated.

2. Experimentation

2.1. *Preparation of the spinel $LiNi_{0.5}Mn_{1.5}O_4$*

The pristine $LiNi_{0.5}Mn_{1.5}O_4$ (LNMO-P) was synthesized using the microwave-assisted chemical co-precipitation method. First, an aqueous solution was prepared by dissolving the 2.775 g manganese sulfate ($MnSO_4$) and 0.8471 g nickel sulfate ($NiSO_4$) in 100 mL deionized water. Later, the solution mentioned above was added with an equimolar volume of sodium carbonate (Na_2CO_3) solution. For homogeneity, the solution was vigorously stirred (1000 rpm) at 80 °C for 12 h, the pH of the solution was kept at 8 with dropwise addition of ammonium hydroxide (NH_4OH) as a chelating agent. Afterward, the solution was diluted with 500 mL of D.I water. Spherical $(Ni_{0.25}Mn_{0.75})CO_3$ precipitation was obtained by

vacuum filtration, cleaned several times with the ammonia solution, and finally washed with water. The obtained spherical particles were heated in the microwave furnace (VBCC HYTHERM, VBCC/MF/14/15) at 550 °C for 15 min by short and repeated irradiation to decompose $(Ni_{0.25}Mn_{0.75})CO_3$. For optimal mixing, a stoichiometric amount of lithium carbonate (Li_2CO_3) was added with the produced material and blended. The precursors were then calcined again with short recurrent irradiation at 800 °C for 15 min. Finally, after cooling to room temperature, black particles were collected. The synthesis of LNMO-P is depicted schematically in Fig. S1(a).

2.2. Preparation of yttria (Y_2O_3) coated $LiNi_{0.5}Mn_{1.5}O_4$

The microwave-assisted chemical precipitation method was used to synthesize pure $LiNi_{0.5}Mn_{1.5}O_4$ (LNMO-YO). First, approximately 0.0121 g $Y(NO_3)_3$ was dissolved in 100 mL of deionized water with continuous stirring. Afterward, the LNMO-P was progressively added to the constantly stirred $Y(NO_3)_3$ aqueous solution at room temperature. The initial pH value was 7, which changed to 9 with the gradual addition of the ammonium hydroxide (NH_4OH) and ammonium chloride (NH_4Cl) buffer solution. Later on, the suspension was ultrasonically dispersed for 2 h. After that, the suspension was heated at 80 °C to collect $LiNi_{0.5}Mn_{1.5}O_4$ precipitates coated with $Y(OH)_3$. Finally, heated with short, repeated irradiation in microwave furnace for 15 min at 600 °C to produce Y_2O_3 coated $LiNi_{0.5}Mn_{1.5}O_4$. The synthesis of LNMO-YO is schematically shown in Fig. S1(b).

2.3. Synthesis of graphene wrapped Y_2O_3 coated $LiNi_{0.5}Mn_{1.5}O_4$

LNMO-YO powder was mixed with 2 wt.% aqueous graphene oxide at room temperature while stirring at a low speed (200 rpm) to produce graphene-wrapped Y_2O_3 coated $LiNi_{0.5}Mn_{1.5}O_4$. The mixture was then sonicated for 30 min for homogenization. The suspension was finally filtered and vacuum dried at 60 °C. The filtrate was then heat-treated in the tube furnace in the presence of argon at 600 °C to cure the coatings. The difference in the dimensions of spherical/quasi-spherical LNMO-YO and graphene nanosheets may not allow the graphene to cover the whole surface of the quasi-spheres but likely to wrap them. This treatment led to obtaining graphene-wrapped Y_2O_3 coated $LiNi_{0.5}Mn_{1.5}O_4$ preserving the original spherical $LiNi_{0.5}Mn_{1.5}O_4$ spinel particles. The synthesis of LNMO-YO-G is schematically shown in Fig. S1(c).

3. Characterization

3.1. Physicochemical characterization

The interstitials and crystal structure configuration of synthesized materials have been examined at a 2°/min scan rate of 0.02 step-size by an X-ray diffractometer (XRD, PANalytical diffractometer). A field emission scanning electron microscope (FE-SEM, Hitachi S-4800) and high-resolution transmission electron microscopy (HR-TEM, JEOL JEM) analyzed the morphologies and microstructures of the samples. Energy-dispersive X-ray spectroscopy (EDX) was used to determine the elemental composition of the developed materials. Thermogravimetric analysis was performed by the TGA analyzer (Pyris 4000, PerkinElmer-USA) to evaluate the thermal stability of the developed materials. The TGA profiles were recorded from 25 °C to 700 °C at a heating rate of 10 °C/min in the presence of nitrogen. XPS (AXIX Ultra DLD, Kratos, U. K) using a monochromatic X-Ray Source – Al Kα source was used to confirm the surface chemical composition. The binding energy of C 1s (284.6 eV) was applied as a reference. The energy resolution was 160 eV, and the spatial resolution was 20 eV.

3.2. Electrode fabrication & electrochemical measurements

Electrochemical experiments were performed utilizing coin-type cells (CR2032). The cathode for the cells was fabricated from a slurry containing 80 wt.% active material, 10 wt.% acetylene black as a conductive agent, and 10 wt.% polyvinylidene fluoride (PVDF) dissolved in n-methyl pyrrolidinone as the binding agent. The slurry was evenly coated on an aluminum foil and dried in a vacuum oven at 120 °C for 12 h. Then, a circular electrode (10 cm in diameter) was punched from the coated foil. The cell assembly was carried out in an argon-filled glove box (H_2O and O_2 content lower than 0.1 ppm) using an ionic separator (Celgard 2325) soaked with 130 mL of the electrolyte solution (1 M LiPF6 in ethyl carbonate (E.C.)/dimethyl carbonate (DMC), 1:1 v/v). The cells were cycled between 3.5 and 4.9 V using WonAtech (WBCS 3000L) battery cycler to study the electrochemical performance. Measurements of the galvanostatic intermittent titration technique (GITT) were recorded at a rate of C/10 using a galvanostatic stage of 10 min and a relaxation time of 1 h. Cyclic voltammetry (CV) was performed using the electrochemical workstation (VSP, BioLogic France) at scanning speeds of 0.05 mV/s. Measurements of electrochemical impedance spectroscopy (EIS) were also obtained on (VSP, BioLogic France) with a 10 mV sinusoidal signal over frequency ranges from 100 kHz to 0.1 Hz. All EIS measurements were performed on samples that had been discharged prior to recording the impedance spectra.

4. Results and discussion

The XRD spectra of the three samples, LNMO-P, LNMO-YO, and LNMO-YO-G, are illustrated in Fig. 1(a). All spectra show the characteristic peak of the LNMO-P structure (JPCD: 01-080-2162). The distinct and sharp peaks confirm that samples are highly pure and crystalline. All Bragg peaks can be indexed to the spinel cubic Fd3m space group, in which the tetrahedral (8a) sites are inhibited by lithium ions and the transition metal ions (Mn and Ni) stay statistically in the octahedral (16d) sites [24], except for a small diffraction peak at 26.2° (Fig. 1(b)). The small diffraction peak at 26.2° associated with carbon confirms the existence of graphene nanosheets. This implies that graphene oxide nanosheets are reduced to graphene nanosheets, packed together, and laminated on the particles before being partially recovered to the ordered form. However, the absence of the Y_2O_3 peak in the XRD spectra can be ascribed to its low content (1%). The lattice constants of the prepared

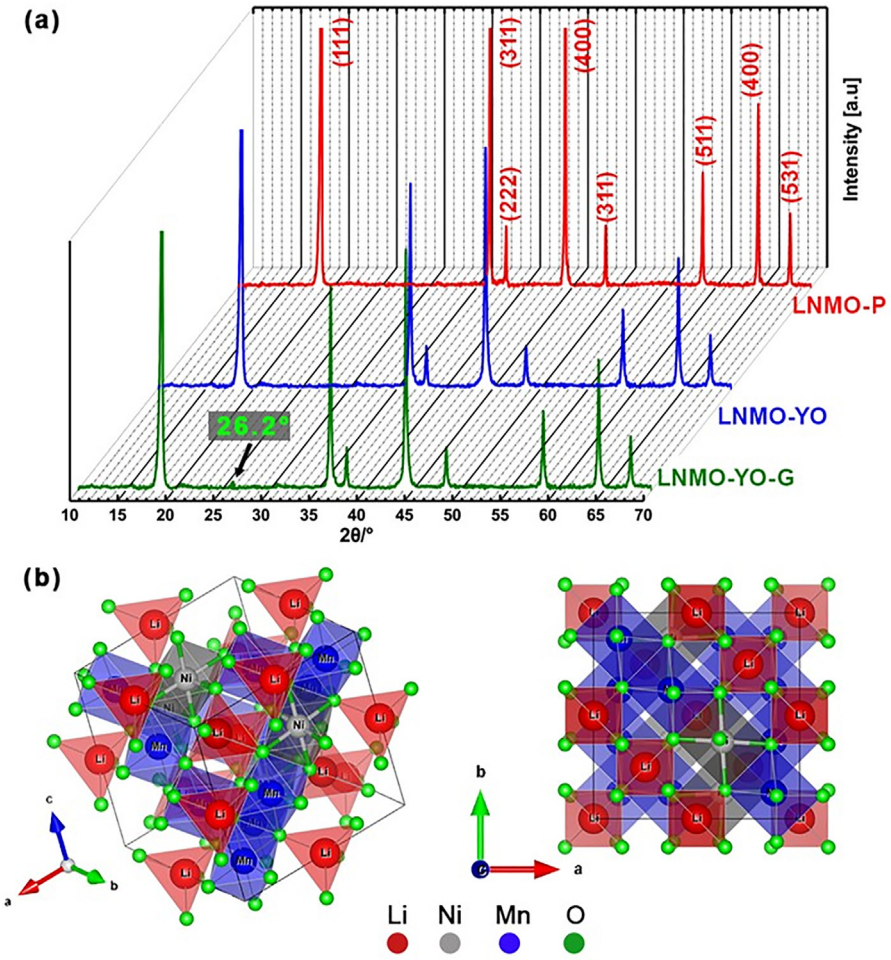

Fig. 1 – (a) XRD spectra of developed materials; LNMO-P, LNMO-YO, and LNMO-YO-G, (b) crystal structure of $LiNi_{0.5}Mn_{1.5}O_4$ in space group Fd3m in which lithium ions occupy the tetrahedral sites 8a, and the transition metal ions (Mn and Ni) reside at the octahedral sites 16d.

materials are shown in Table 1. The value of the lattice constant suggests that Y_2O_3 coating and subsequent graphene wrapping of LNMO-P did not penetrate the spinel system but are merely mounted on the particle surface, indicated by a small change in the lattice constant. It also suggests that the designed and optimized heat treatment would not modify the parent spinel structure of LNMO-P.

X-ray Photoelectron Spectroscopy (XPS) was carried out to analyze the surface chemistry, particularly Y_2O_3 coating and the oxidation states of transition metals present in the synthesized materials. The XPS spectra of Ni-2p, Mn-2p, and Y-3d of LNMO-P, LNMO-YO, and LNMO-YO-G powders are shown in Fig. 2. The XPS spectra were fitted using XPS-PeaksFit software to evaluate the transition metals' oxidation state. The high-resolution XPS spectra for yttrium (Y) suggests the absence of Y_2O_3 coating on LNMO-P, while it confirms yttrium (Y) presence in LNMO-YO and LNMO-YO-G, signals of binding energy from the Y-$3d_{3/2}$ (Y_2O_3, 157.45 eV) and Y-$3d_{5/2}$ (Y_2O_3, 155.52 eV). Two peaks of Ni-$2p_{1/2}$ at 872.77 ± 0.20 eV and Ni-$2p_{3/2}$ at 854.82 ± 0.10 eV are displayed by all powder samples. For all the samples, the Ni-2p spectrum displays signals of Ni-$2p_{3/2}$ with binding energies of 854.0 eV, referring to the Ni^{2+} oxidation state [30]. The binding energy of Ni-$2p_{3/2}$ is 855.4 eV, and the satellite peak is 861 eV, both of which are typical of Ni^{2+} [31]. It should be noted that the binding energy of the MnLVV Auger transition with Alk excitation is quite near to the peak of Ni2p3/2; the mentioned peak is deconvoluted to Ni$2p_{3/2}$ peak with the satellite [32]. For manganese (Mn), two signals that can be ascribed to Mn-2p are seen in the range, Mn-$2p_{3/2}$ at 641–642 eV and Mn-$2p_{1/2}$ at 652–654 eV. The Mn-$2p_{3/2}$ signals are used for the assessment of the surface oxidation state of Mn. The Mn-$2p_{3/2}$ signal with a binding energy of 642.5 eV corresponds to Mn^{4+}, and the other signal with a binding energy of 641.6 eV corresponds to Mn^{3+}. The sample of LNMO-P shows Mn-$2p_{3/2}$ at 641.6 eV, suggesting that the major oxidation state of Mn ions is

Table 1 – Lattice parameters for LNMO-P, LNMO-YO, and LNMO-YO-G.

Sample	Lattice constant (Å)	Volume (Å^3)
LNMO-YO-G	8.16	543.338
LNMO-YO	8.18	547.343
LNMO-P	8.21	553.387

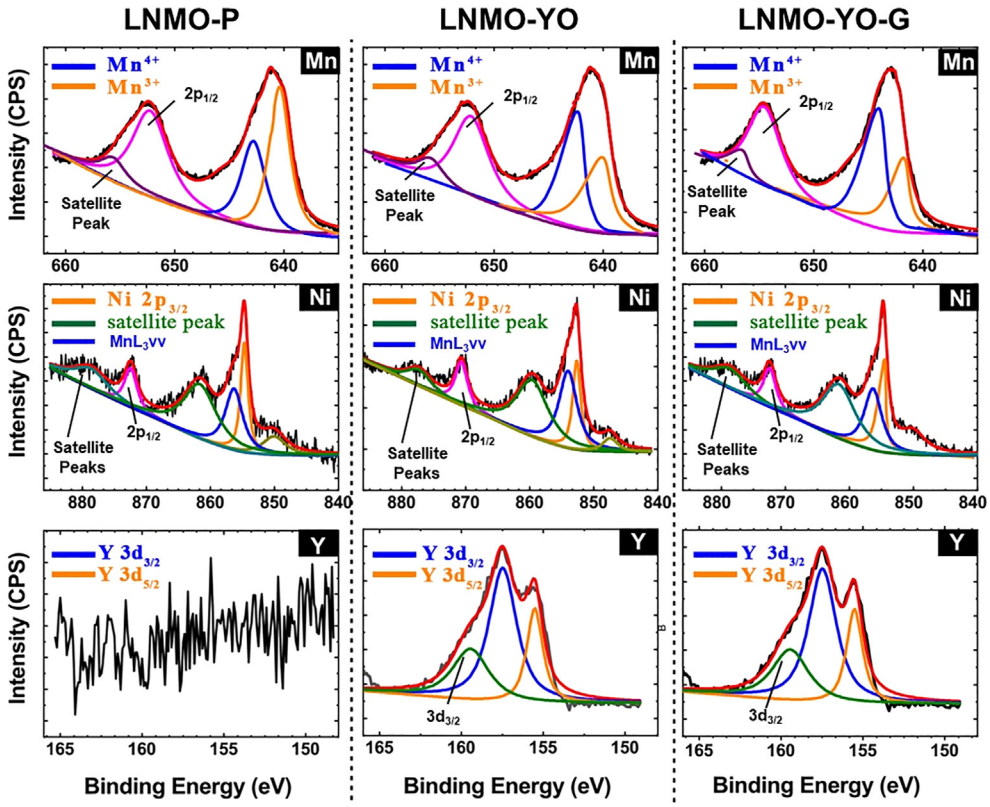

Fig. 2 – High-resolution XPS spectra of LNMO-P, LNMO-YO, and LNMO-YO-G samples.

Mn^{3+}, but the peak separation of Mn-$2p_{3/2}$ peak achieves a modest contribution of Mn^{4+}, it can be assumed that due to higher intensity of Mn^{3+}, LNMO-P sample will suffer from Jahn Teller Distortion [33]. However, LNMO-YO and LNMO-YO-G samples display peaks of Mn-$2p_{1/2}$ at 654.42 ± 0.28 eV and Mn-$2p_{3/2}$ at 642.66 ± 0.10 eV, which are compatible with the existence of Mn^{4+}. It can be assumed that the presence of Y_2O_3 and graphene in the structure of LNMO-P suppress the existence of Mn^{3+} and promote the stability of Mn^{4+}. These results agree with the previous studies [34] and electrochemical characterization data of Fig. 6(a).

Thermal gravimetric analysis was used to evaluate the prepared materials' thermal stability and estimate the amount of carbon. The sample weight shift was tracked as a function of temperature, which produced a difference in graphene concentration. As seen in Fig. S2, LNMO-P and LNMO-YO samples do not display any detectable weight loss during the entire heating range. However, the LNMO-YO-G sample shows some weight loss when heated from room temperature (25 °C) to 700 °C. The TGA plot of the LNMO-YO-G sample reveals two weight reduction areas. Till 150 °C, the first weight loss area is the moisture loss relating to the water's evaporation in the powder sample. The second weight-loss area extends to 700 °C, which illustrates carbon degradation. The maximum weight loss is only 3% in the entire heating range. The overall calculated carbon loss for the LNMO-YO-G sample in the studied temperature range is 2.0%. Moreover, all three developed materials (LNMO-P, LNMO-YO, and LNMO-YO-G) demonstrate good thermal stability till 700 °C.

The FE-SEM images of LNMO-P, LNMO-YO, and LNMO-YO-G are presented in Fig. 3. The LNMO-P retains the inherent spherical morphology, even after high-temperature microwave calcination.

The LNMO-P sample is made up of quasi-spheres, having a size of 2–5 μm diameter. However, several minor holes on the LNMO-P particles' surface can be found, possibly triggered by CO_2 escape during the calcination process. In comparison, the FE-SEM images of LNMO-P and LNMO-YO do not differ considerably, as the coating thickness is in the nanometric range (Fig. 3(a and b)). For the LNMO-YO-G sample, the surface of LNMO-YO coated particles is partially enveloped by graphene; its wrinkled layer bears the morphology of nanosheets (Fig. 3(c)).

EDX analysis of the LNMO-YO-G sample is shown in Fig. 4(a), which confirms the presence of elements constituting the developed materials. Furthermore, the elemental mapping of the sample (Fig. 4(b)) explicitly shows that "C" and "Y" have the same distribution as the Ni, Mn, and O.

Further, it also suggests that LNMO-P spherical particles are covered uniformly with Y_2O_3. The EDX analysis indicates that LNMO-P particles have been successfully coated with Y_2O_3 and wrapped with graphene nanosheets. The uniform Y_2O_3 nano-coating is expected to avoid unnecessary interaction between the electrolyte and the electrode interface, thus may increase the cycling performance. In addition, the nanoscale coating would not obstruct the internal pathways so that the performance is not hindered. The LNMO-YO-G microspheres consist of internal radial channels and provide

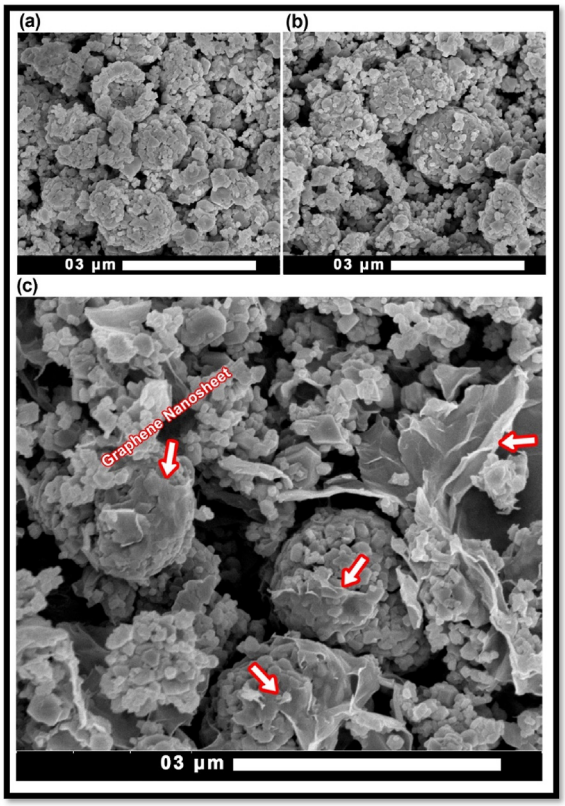

Fig. 3 – FE-SEM micrographs of the prepared materials; (a) Pristine $LiMn_{1.5}Ni_{0.5}O_4$ particles (b) Yttria coated $LiMn_{1.5}Ni_{0.5}O_4$ particles (c) Yttria coated $LiMn_{1.5}Ni_{0.5}O_4$ particles partially wrapped by graphene sheets, marked by arrows.

a controlled electrolyte wettability, improved electronic conductivity, and protection from ionic leaching.

High-resolution transmission electron microscopy (HR-TEM) has been carried out to validate the existence of the Y_2O_3 coatings and graphene nanosheets on the surface of LNMO-P particles. Fig. 5(a) shows HR-TEM micrographs, lattice fringes (d = 0.476 nm) with corresponding SAED patterns of the LNMO-YO-G sample. The LNMO-P sample particles show a smooth appearance (Fig. S3), but the gritty nature of the LNMO-YO and LNMO-YO-G may be due to a nanofilm that could be Y_2O_3 and multilayer graphene. On the outer surface of LNMO-YO & LNMO-YO-G, it is evident that the nano-Y_2O_3 coating has a thickness of around 6–8 nm. Thus, the Y_2O_3 coatings will avoid the direct interaction between the active material and the electrolyte, thereby reducing the undesired reactions with the electrolyte. The existence of graphene improves the electrical conductivity of the spinel $LiMn_{1.5}Ni_{0.5}O_4$, enhancing electrochemical performance. In general, the increase in the thickness of the Y_2O_3 coating is followed by a sharp increase in contact resistance and load transfer resistance, especially when the coating is thicker than 10 nm [35]. In the present study, the Y_2O_3 coating thickness is 5–8 nm, ensuring the successful circumvention of polarization and power depletion.

The SAED pattern (Fig. 5(b)) of one independent LNMO-YO-G particle shows its unique nature; higher crystallinity results in a decreased energy barrier for Li^+ ions insertion, enabling a more comfortable and faster diffusion of the Li^+ ions. It can be further noticed that the divide between lattice fringes is 0.478 nm, which corresponds to the LNMO-P (111) plane's interplanar division in conjunction with the XRD data. Thus, based on EDX analysis and SAED patterns, it can be concluded

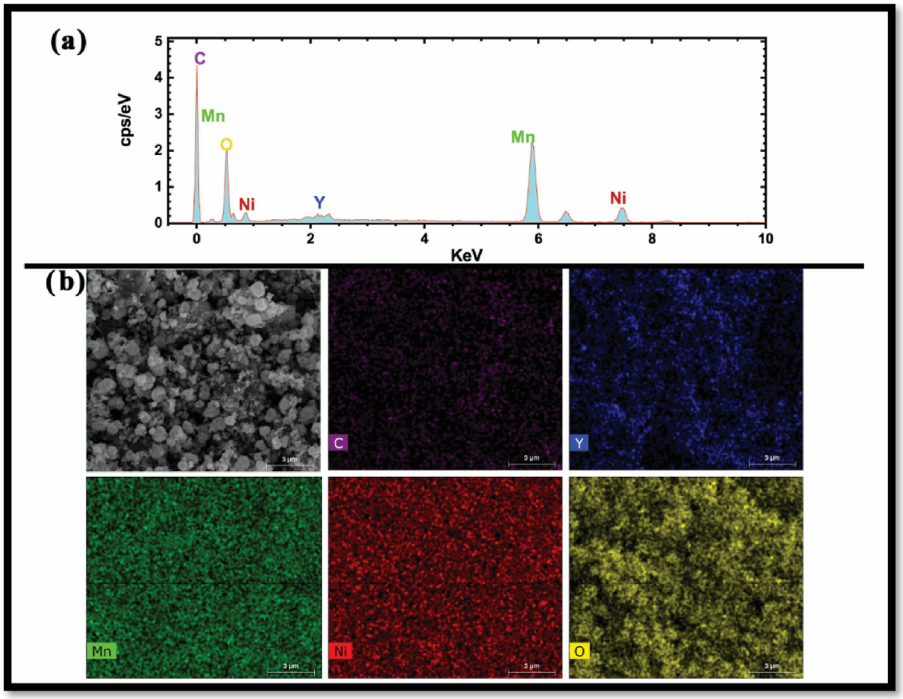

Fig. 4 – (a) EDX analysis of LNMO-YO-G sample, (b) EDX elemental mapping of LNMO-YO-G particles.

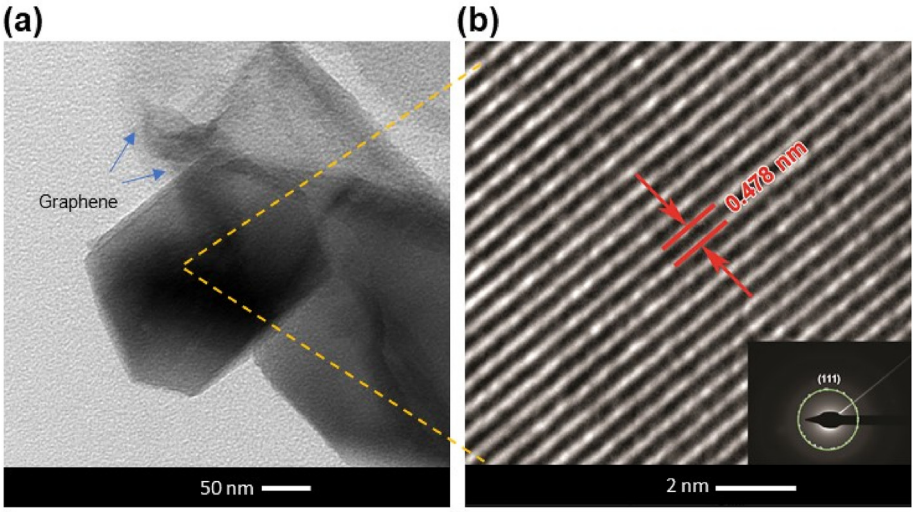

Fig. 5 – (a) HR-TEM micrographs of graphene wrapped particles of LNMO-YO-G sample (b) lattice fringes (d = 0.476 nm) with corresponding SAED patterns of LNMO-YO-G sample.

that high-phase purity materials are prepared through microwave-assisted chemical co-precipitation technique.

Fig. S4 illustrates the protective mechanism of protective coatings schematically. The coatings protect the particles from ionic leaching (Jahn-Teller effect) and unwanted reactions with the electrolyte. The coated surface on the right is protected from unwanted parasitic reactions at the electrode/electrolyte interface. In contrast, the uncoated surface suffers from degradation of the electrode due to ionic leaching and other unwanted chemical reactions.

Fig. 6(a) shows the rate capability of LNMO-P, LMO-YO, and LNMO-YO-G sample cells. To examine the performance of increasing the current rate, the cells were charged and discharged from 0.1C to 10C between 3.5 V and 4.9 V. Different capacities are obtained, which can be attributed to the various current rate applied and the governing electrochemical

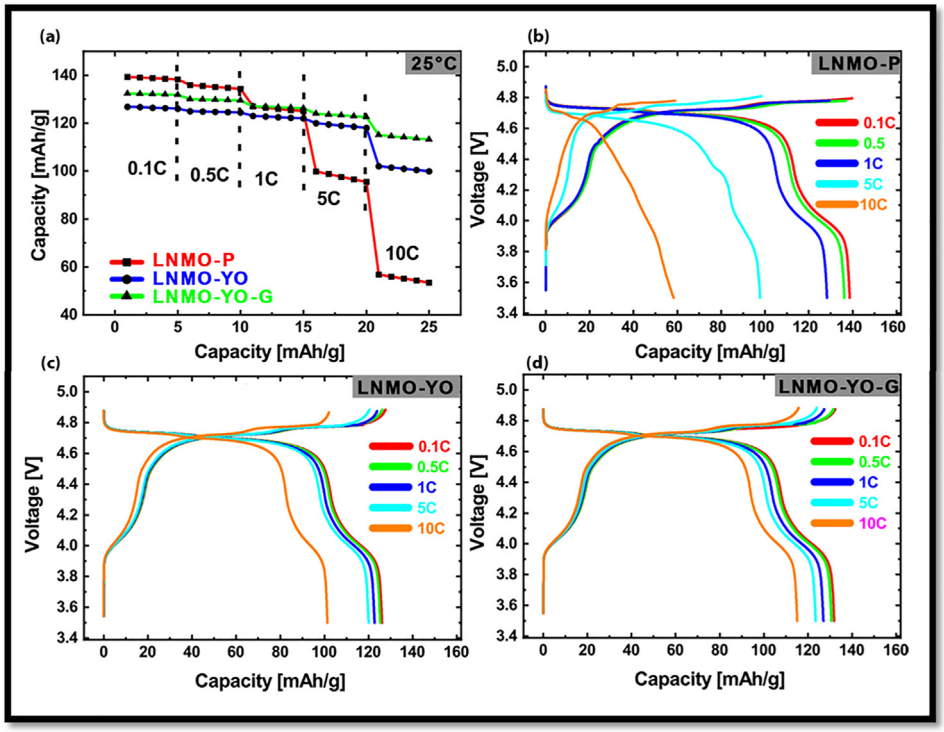

Fig. 6 – (a) Rate capability of LNMO-P, LNMO-YO, and LNMO-YO-G at 25 °C, Galvanostatic charge/discharge curves at different C-rates of (b) LNMO-P (c) LNMO-YO (d) LNMO-YO-G.

processes contributing to deteriorating the efficiency of the cells. The discharge capacity of the LNMO-P cell is drastically decreased from 139 mAh g^{-1} at 0.5C to 99.8 mAh g^{-1} at 5C and 55.3 mAh g^{-1} at 10C rate (Fig. 6(b)). However, the LNMO-YO and LNMO-YO-G cells offer higher discharge capacities of 120 mAh g^{-1} and 126 mAh $g^{-1,}$ respectively, at 5C. More importantly, a remarkable improvement in the discharge behavior of LNMO-YO and LNMO-YO-G cells is noticed at 10 C, exhibiting discharge capacities of 102 mAh g^{-1} and 115 mAh $g^{-1,}$ respectively (Fig. 6(c and d)). The rate capacity results suggest that the electrochemical performance of cathode materials at higher C-rates can be restricted by resisting the charge transfer at the electrode/electrolyte interface or lithium-ion mobility [35].

The findings indicate that the increased discharge capacity of LNMO-YO and LNMO-YO-G may be due to the Y_2O_3 coating and wrapping of LNMO-YO particles in graphene nanosheets. This can be attributed to the direct effect of graphene to boost electronic conductivity and reduce the diffusion path of lithium ions [36]. Furthermore, the LNMO-YO and LNMO-YO-G sample cells display excellent discharge stability and no evident deterioration at each current input (C-rate) level compared to the LNMO-P. Therefore, it can be concluded that Y_2O_3 coating and wrapping of LNMO-YO particles in graphene nanosheets have effectively improved the cycling efficiency of LNMO-P at all C-rates, especially at the high C-rates.

Fig. 7 demonstrates the constant current charge/discharge behavior of the LNMO-P, LNMO-YO, and LNMO-YO-G cells operated between 3.5 V and 4.9 V at 0.1C. As the cycles progress, the lithium intercalation can be traced to the two-stage extraction process; the charging plateau moves upwards to higher potential due to the polarization of the cathode, while the discharge plateau drops down to lower potential. The redox processes resulted in one plateau at ~4.0 V corresponding to the Mn^{3+}/Mn^{4+} pair and the other dominant at ~4.7 V resulting from a redox pair Ni^{2+}/Ni^{4+}. Initially, the LNMO-P cell (Fig. 7(a)) shows a higher discharge capacity than LNMO-YO and LNMO-YO-G cells.

Although it has a high discharge capacity of 139 mAh g^{-1} at first discharge possessing well-defined plateaus, it loses its discharge capacity to 114 mAh g^{-1} at 0.1C after 100 cycles. It is reported that capacity in the first cycle is generally overlooked since permanent power loss occurs at many separate positions during this phase. The most significant factor for this cause is forming a solid electrolyte interface (SEI) layer, the cathode/electrolyte interface [37]. As a result, the LNMO-YO-G cell has a discharge capacity of 131 mAh g^{-1} after 100 cycles, whereas the LNMO-YO and LNMO-P have 124 mAh g^{-1} and 114 mAh g^{-1} respectively, after 100 cycles. Additionally, the LNMO-YO-G cell also demonstrates an improved discharge capacity retention of 98.6% compared to LNMO-YO (96.7%) and LNMO-P (81%) after 100 cycles, again confirming the usefulness of Y_2O_3 coating and graphene wrapping constituting the novel structure of the LNMO-YO-G sample.

The electrochemical activity of the redox pairs was estimated using cyclic voltammetry (CV). Fig. 8(a) compares the CV curves of LNMO-P, LNMO-YO, and LNMO-YO-G. The dominant peaks at 4.7 V are due to the redox pair of $Ni^{2+}/Ni^{4+,}$ and other peaks 4.0 V can be attributed to the redox pair of Mn^{3+}/Mn^{4+}. By comparing the peak area at 4.0 V, the peak intensity of Mn^{3+}/Mn^{4+} redox couple in LNMO-P is greater than that of LNMO-YO and LNMO-YO-G, corresponding with the initial discharge potential. In contrast to LNMO-P and LNMO-Y, the Ni^{2+}/Ni^{4+} redox couple is more prominent for the LNMO-YO-G, and an opposite trend is noticed in the case for Mn^{3+}/Mn^{4+} redox couple. These findings suggest a higher Mn^{3+} contribution in

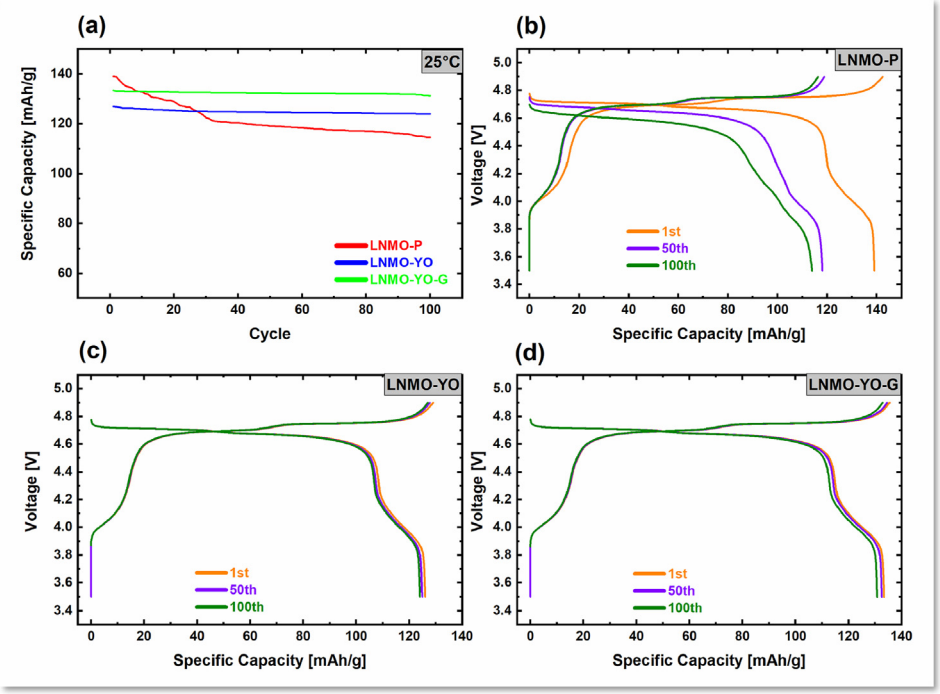

Fig. 7 – (a) Cyclability of LNMO-P, LNMO-YO, and LNMO-YO-G, galvanostatic charge/discharge behavior, (b) LNMO-P, (c) LNMO-YO, and (d) LNMO-YO-G.

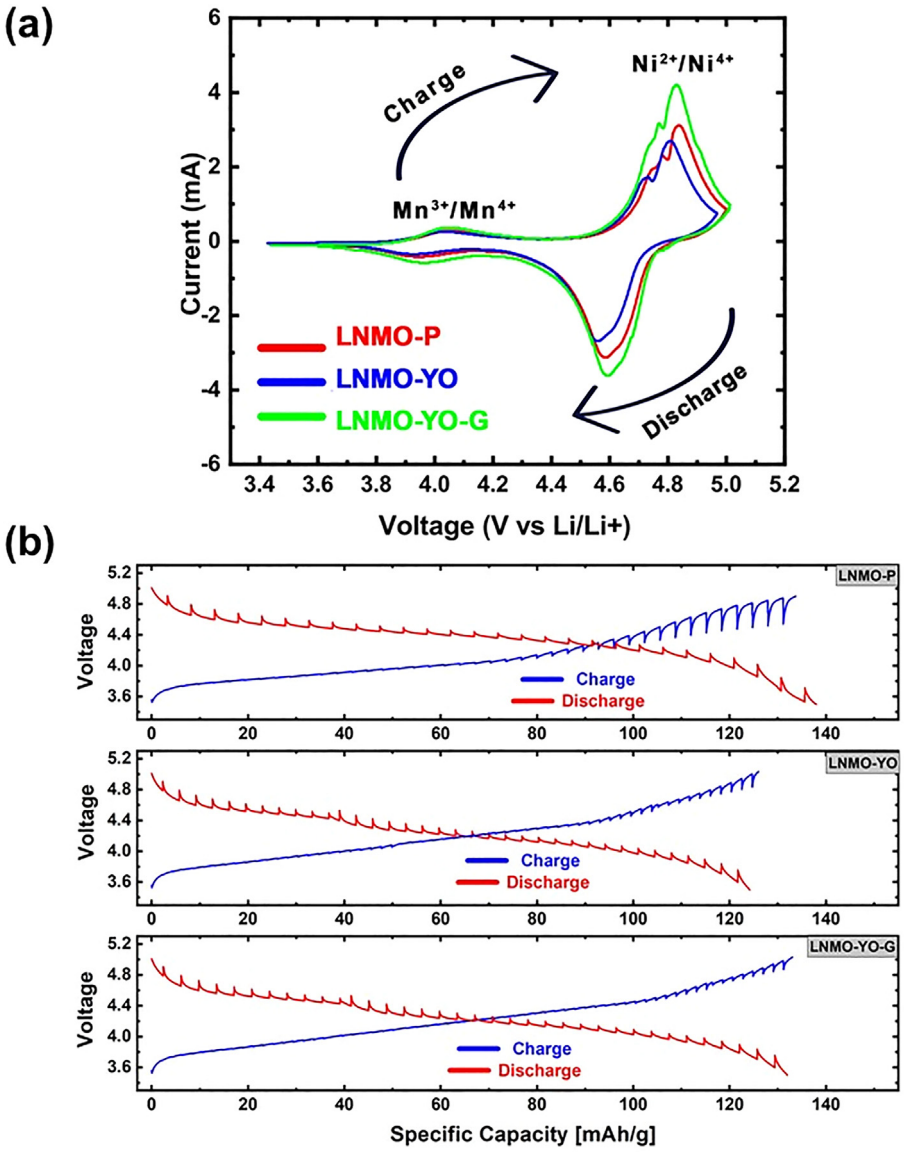

Fig. 8 – (a) Comparison of cyclic voltammetry (CV) of LNMO-P, LNMO-YO, and LNMO-YO-G scanned at 0.05 mV/s, (b) GITT curves of LNMO-P, LNMO-YO, and LNMO-YO-G sample cells measured at the C/10 rate between 3.5 V and 4.9 V.

LNMO-P, which is consistent with XPS results. Furthermore, the peak-to-peak differentiation is more significant for the LNMO-YO-G cell, which implies that LNMO-YO-G shows better electrochemistry and quicker intercalation kinetics.

Galvanostatic Intermittent Titration (GITT) measurements were carried out to get an insight into the electrochemical behavior of developed cathode materials. The cells were charged/discharged in steps disrupted by rest periods to provide ample time for possible equilibrium [38,39]. As illustrated in Fig. 8(b), measurements were recorded at C/10 to obtain the quasi-equilibrium profile for the reaction kinetics. The comparison of GITT curves of LNMO-P, LNMO-YO, and LNMO-YO-G samples indicate a smoother intercalation/de-intercalation of lithium due to the negligible over potential or polarization in the voltage window of Ni^{2+}/Ni^{4+} redox couple.

Lithium-ions in the LNMO-P spinel exist in 8a sites and move in 8a-16c diffusion tracks across the empty octahedral of 16c sites. An increase in the applied voltage has resulted in slower lithium diffusion due to the large polarization in LNMO-P, ascribed to $Ni^{2+/3+}$ and $Ni^{3+/4+}$ redox couples. However, the $Ni^{2+/3+}$ and $Ni^{3+/4+}$ redox pairs lead to smoother OCV profiles in LNMO-Y and LNMO-G-Y. Compared to the pure LNMO-P, the brief relaxation spikes observed for the LNMO-YO and LNMO-YO-G showing rapid reaction kinetics with a limited polarization and fast equilibration. Until lithium is 70% extracted, the smoother intercalation/de-intercalation of lithium in the LNMO-YO and LNMO-YO-G shows more electrochemical activity in these cathode materials. During the charging, the relaxation spikes are lower, suggesting that the oxidation phase is outperforming. The oxidation peak areas are comparatively more significant than those of the reduction peak areas and are supported by the asymmetry of the oxidation and reduction as shown in CV curves.

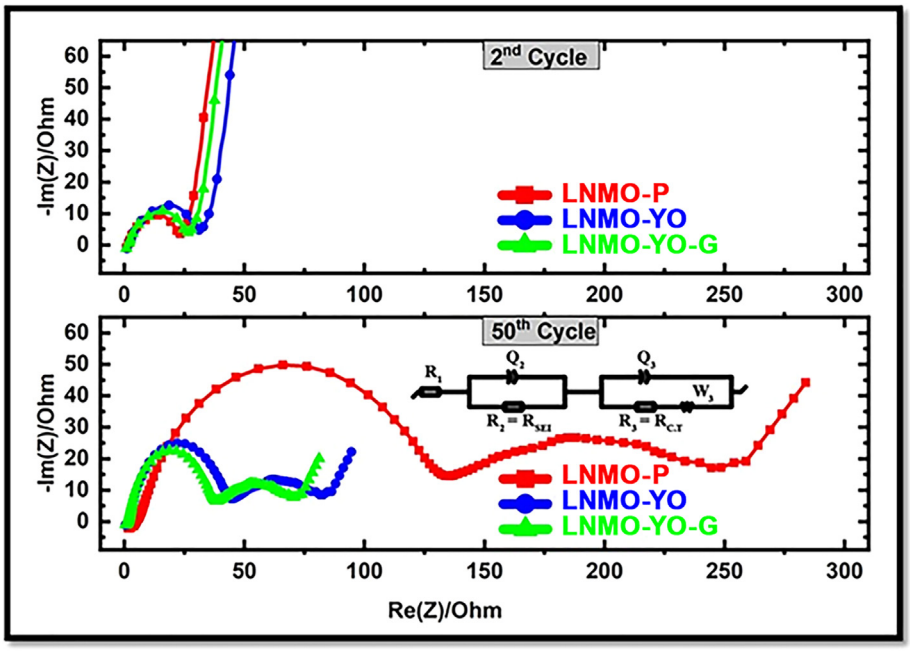

Fig. 9 – The Nyquist plot of LNMO-P, LNMO-YO, and LNMO-YO-G samples obtained after 50 cycles under constant current charge–discharge between 3.4 V and 4.9 V at C/10 rate at 25 °C.

Electrochemical impedance spectroscopic analysis of the prepared materials after the 2nd and 50th cycles is reported to understand better the beneficial impact of Y_2O_3 coating and the graphene nanosheets wrapping around LNMO-P particles. The Nyquist plot of LNMO-P, LNMO-YO, and LNMO-YO-G samples obtained after fitting with the corresponding circuit are shown in Fig. 9.

The Nyquist plots comprise three significant areas. Usually, a half-circle of the impedance spectra in the high-frequency range is due to the development of the formation of the solid electrolyte interphase or interfacial resistance (R_{SEI}); the low-frequency semicircle is due to an impedance of the charge transfer (C.T) from the electrode to electrolyte interface (R_{CT}) [40,41]. Finally, in the low-frequency region, the

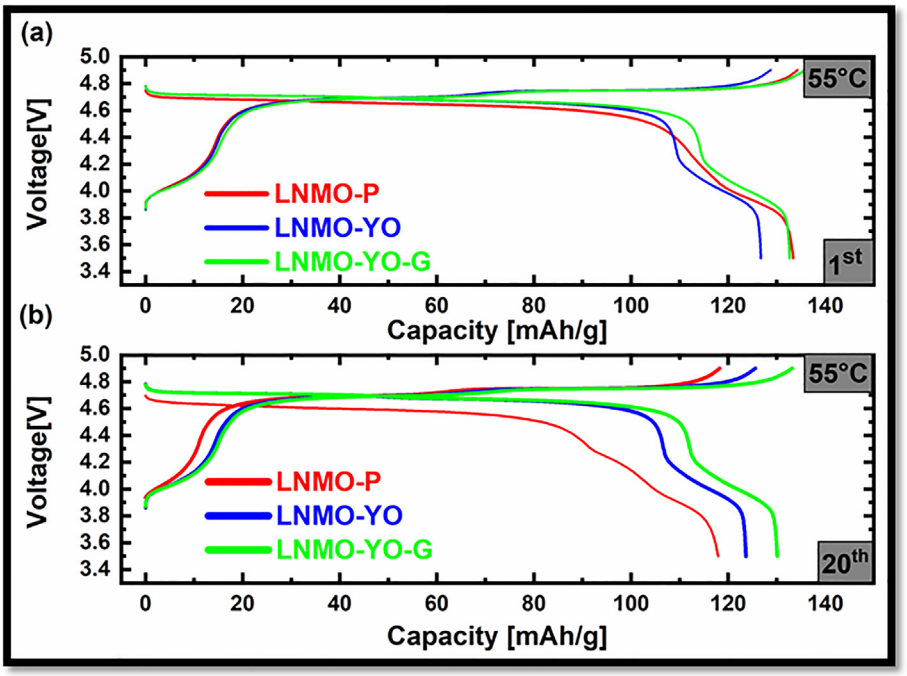

Fig. 10 – Constant current cycling at 0.1C and elevated temperature (55 °C) (a) 1st cycle (b) 20th cycle.

oblique line represents the Warburg impedance (Wo), which relates to the diffusion of Li^+ in the bulk of the electrode [42]. The LNMO-P cell has the lowest initial resistance due to the high content of Mn^{3+}, as illustrated by XPS analysis. However, with increasing the number of cycles, the impedance of the LNMO-P cell significantly rises (R_{SEI} = 131 Ω). An increase in the impedance value suggests the decrease in the electrochemical stability of LNMO-P, which can be attributed to the parasitic reactions between the LNMO-P particles and the liquid electrolyte. The interaction of LNMO-P particles with the electrolyte leads to the continuous development of the undesired SEI layer that is immune to ionic conduction and thus results in degradation of intercalation kinetics [43].

Conversely, after the 50th cycle, the shift in impedance for the LNMO-YO (R_{SEI} = 39 Ω) and LNMO-YO-G (R_{SEI} = 27 Ω) is remarkably lower than that of the pristine LNMO (R_{SEI} = 131 Ω), indicating that the Y_2O_3 coating and graphene nanosheets wrapping of LNMO-P has circumvented the parasitic reactions between the electrolyte and active electrode material, suggesting the beneficial role of novel structure. Consequently, the formation of an unfavorable SEI layer is retarded, and the kinetics of charge transfer has not deteriorated, leading to a significant increase in the battery's electrochemical efficiency. These results are also consistent with previous studies [44–46].

The cyclability and high-temperature galvanostatic charge/discharge behavior of LNMO-P, LNMO-YO, and LNMO-YO-G samples were studied at 55 °C, as shown in Fig. 10. The discharge capacity of pristine LNMO-P degrades over 20 cycles from 133 mAh g^{-1} to 108 mAh g^{-1} indicating capacity retention of 81%. In comparison, the discharge capacity of the LNMO-YO declines from 126 mAh g^{-1} to 122 mAh g^{-1} after 20 cycles showing capacity retention of 96% retention. Remarkably, the discharge capacity of the LNMO-YO-G declines from 134 mAh g^{-1} to 132 mAh g^{-1} after 20 cycles showing capacity retention of 98% retention. Well-defined redox plateau with a significant separation compared to others (observed in LNMO-YO-G) may be attributable to the excellent dispersion of graphene nanosheets and suitable establishment of pathways to allow more comfortable transport of electrons.

Moreover, a comparison of discharge profiles at 55 °C of LNMO-P, LNMO-YO, and LNMO-YO-G clearly shows the enhancement of high-temperature performance of LNMO-P by Y_2O_3 coatings and graphene nanosheets wrapping, revealing their suitability under harsh conditions. The capacity fading of LNMO-P can be attributed partly to the loss of transition elements at elevated temperatures (55 °C), as the length of the voltage plateaus decreases continually [47]. This is consistent with the generally witnessed dissolution of manganese and subsequent structural deterioration of the active material [48], as illustrated earlier in Fig. 7. The decreased dissolution of transition metals due to Y_2O_3 coating and wrapping of graphene nanosheets has ensured the improved electrochemical performance of LNMO. It is, therefore, confirmed that the presence of Y_2O_3 coating and graphene wrapping serves as a defensive layer against parasitic reactions. The significant improvement in electrochemical performance indicates that the proposed synthesis strategy is an effective way of increasing the electrochemical performance of $LiNi_{0.5}Mn_{1.5}O_4$.

5. Conclusion

Using microwave-assisted chemical co-precipitation, quasi spheres of pristine $LiMn_{1.5}Ni_{0.5}O_4$ (LNMO-P), Y_2O_3 coated $LiMn_{1.5}Ni_{0.5}O_4$ (LNMO-YO), and Y_2O_3 coated $LiMn_{1.5}Ni_{0.5}O_4$ wrapped in graphene nanosheets (LNMO-YO-G) was synthesized. The presence of Y_2O_3 coating and the wrapping of graphene nanosheets significantly influence the electrochemical performance of LNMO-P. The designed cathode material architecture has resulted in remarkable cycling efficiency, capacity retention, and rate capability. After 100 cycles between 3.5 V and 4.9 V, the Y_2O_3 coated $LiMn_{1.5}Ni_{0.}5O_4$ wrapped in graphene nanosheets has the maximum discharge capacity of 131 mAh g^{-1} at 0.1 C, capacity retention of 98.4% after 100 cycles, but discharge capacity of pure $LiMn_{1.5}Ni_{0.5}O_4$ is only 114 mAh g^{-1} with 82.3% efficiency. This improvement electrochemical performance is due to (i) circumvention of the parasitic reactions between the electrolyte and active electrode material due to Y_2O_3 coating and graphene nanosheets wrapping of LNMO-P, (ii) retardation of the formation of an unfavorable SEI layer, (iii) prevention of Mn^{3+} dissolution due to the Jahn Teller effect, and (iv) improvement in the kinetics of charge transfer. Besides, even at higher discharge rates of 5 C and 10 C, the LNMO-YO-G delivered a significantly higher discharge capacity of 125 mAh g^{-1} and 117 mAh g^{-1}. The discharge capacity of pristine LNMO-P degrades over 20 cycles from 133 mAh g^{-1} to 108 mAh g^{-1} indicating capacity retention of 81%. In comparison, the discharge capacity of the LNMO-YO-G declines from 134 mAh g^{-1} to 132 mAh g^{-1} after 20 cycles showing capacity retention of 98% retention. The comparison of discharge profiles at 55 °C clearly shows the enhancement of high-temperature performance of LNMO-P by Y_2O_3 coatings and graphene nanosheets wrapping. The proposed material architecture suppresses the parasitic reactions and thus improves the cyclic stability of the cathode. The Y_2O_3 coating and then wrapping graphene over the quasi-spherical surface of $LiMn_{1.5}Ni_{0.5}O_4$ is an efficient approach to increase both the cycle stability and rate performance of $LiMn_2O_4$. The reported material development concept can be effectively extended to other families of cathode materials.

Declaration of Competing Interest

The authors declare that they have no known competing financial interests or personal relationships that could have appeared to influence the work reported in this paper.

Acknowledgments

This publication was made possible by NPRP Grant # NPRP11S-1225-170128 from Qatar National Research Fund (a member of the Qatar Foundation). This publication was also made possible by the Qatar University Internal Grant (QUCG-CENG-20/21-2). Open Access funding provided by the Qatar National Library. Statements made herein are solely the responsibility of the authors. Microstructural analyses (FE-SEM/EDX and HR-

TEM) were accomplished at the Central Laboratory Unit (CLU), Qatar University, Doha, Qatar. XPS analysis was accomplished at the Gas Processing Center (GPC), Qatar University, Doha, Qatar.

Appendix A. Supplementary data

Supplementary data to this article can be found online at https://doi.org/10.1016/j.jmrt.2021.07.038.

REFERENCES

[1] Deng D. Li-ion batteries: basics, progress, and challenges. Energy Sci Eng 2015;3(5):385–418. https://doi.org/10.1002/ese3.95.

[2] Manley JB, Anastas PT, Cue BW. Frontiers in Green Chemistry: meeting the grand challenges for sustainability in R&D and manufacturing. J Clean Prod 2008;16(6):743–50. https://doi.org/10.1016/j.jclepro.2007.02.025.

[3] James Abraham J, Arro CRA, Tariq HA, Kahraman R, Al-Qaradawi S, Al tahtamouni TM, et al. Sodium and lithium incorporated cathode materials for energy storage applications - a focused review. J Power Sources 2021;506:230098. https://doi.org/10.1016/j.jpowsour.2021.230098.

[4] Suo Z. Reactive flow in large-deformation electrodes of lithium-ion batteries. Int J Appl Mech 2012;4(3). https://doi.org/10.1142/S1758825112500238.

[5] Delacourt C, Poizot P, Levasseur S, Masquelier C. Size effects on carbon-free LiFePO4 powders. Electrochem Solid State Lett 2006;9(7). https://doi.org/10.1149/1.2201987.

[6] Ben L, Yu H, Chen B, Chen Y, Gong Y, Yang X, et al. Unusual spinel-to-layered transformation in LiMn 2 O 4 cathode explained by electrochemical and thermal stability investigation. ACS Appl Mater Interfaces 2017;9(40):35463–75. https://doi.org/10.1021/acsami.7b11303.

[7] Agubra V, Fergus J. Lithium ion battery anode aging mechanisms. Materials (Basel) 2013;6(4):1310–25. https://doi.org/10.3390/ma6041310.

[8] Kim JW, Kim DH, Oh DY, Lee H, Kim JH, Lee JH, et al. Surface chemistry of LiNi0.5Mn1.5O4 particles coated by Al2O3 using atomic layer deposition for lithium-ion batteries. J Power Sources 2015;274:1254–62. https://doi.org/10.1016/j.jpowsour.2014.10.207.

[9] Ma SB, Nam KW, Yoon WS, Bak SM, Yang XQ, Cho BW, et al. Nano-sized lithium manganese oxide dispersed on carbon nanotubes for energy storage applications. Electrochem Commun 2009;11(08):1575–8. https://doi.org/10.1016/j.elecom.2009.05.058.

[10] Wang G, Wen W, Chen S, Yu R, Wang X, Yang X. Improving the electrochemical performances of spherical LiNi0.5Mn1.5O4 by Fe2O3 surface coating for lithium-ion batteries. Electrochim Acta 2016;212:791–9. https://doi.org/10.1016/j.electacta.2016.07.025.

[11] Li S, Zhu K, Zhao D, Zhao Q, Zhang N. Porous LiMn2O4 with Al2O3 coating as high-performance positive materials. Ionics (Kiel) 2019;25(5):1991–8. https://doi.org/10.1007/s11581-018-2643-y.

[12] Lee SW, Kim KS, Moon HS, Kim HJ, Cho BW, Cho W Il, et al. Electrochemical characteristics of Al2O3-coated lithium manganese spinel as a cathode material for a lithium secondary battery. J Power Sources 2004;126(1–2):150–5. https://doi.org/10.1016/j.jpowsour.2003.08.032.

[13] Arumugam D, Paruthimal Kalaignan G. Synthesis and electrochemical characterizations of Nano-SiO2-coated LiMn2O4 cathode materials for rechargeable lithium batteries. J Electroanal Chem 2008;624(1–2):197–204. https://doi.org/10.1016/j.jelechem.2008.09.007.

[14] Nisar U, Amin R, Essehli R, Shakoor RA, Kahraman R, Kim DK, et al. Extreme fast charging characteristics of zirconia modified LiNi0.5Mn1.5O4 cathode for lithium ion batteries. J Power Sources 2018;396:774–81. https://doi.org/10.1016/j.jpowsour.2018.06.065.

[15] Li C, Zhang HP, Fu LJ, Liu H, Wu YP, Rahm E, et al. Cathode materials modified by surface coating for lithium ion batteries. Electrochim Acta 2006. https://doi.org/10.1016/j.electacta.2005.11.015.

[16] Shakoor RA, Abraham JJ, Monawwar H, Quddus AA, Tariq H, Saleh I, et al. Synthesis and performance evaluation of SiO_2 coated Li-rich $Li_{1.2}Ni_{0.13}Mn_{0.54}Co_{0.13}O_2$ cathode materials for Li-ion batteries. ECS Meet Abstr 2020;MA2020-01(2):399. https://doi.org/10.1149/MA2020-012399mtgabs.

[17] Deng YF, Zhao SX, Xu YH, Nan CW. Effect of the morphology of Li-La-Zr-O solid electrolyte coating on the electrochemical performance of spinel LiMn1.95Ni0.05O3.98F0.02 cathode materials. J Mater Chem A 2014;2(44):18889–97. https://doi.org/10.1039/c4ta03772c.

[18] Deng YF, Zhao SX, Hu DH, Nan CW. Structure and electrochemical performance of spinel LiMn 1.95Ni0.05O3.98F0.02 coated with Li-La-Zr-O solid electrolyte. J Solid State Electrochem 2014;18(1):249–55. https://doi.org/10.1007/s10008-013-2265-2.

[19] Cui X, Lee VA, Raphael Y, Wiler JA, Hetke JF, Anderson DJ, et al. Surface modification of neural recording electrodes with conducting polymer/biomolecule blends. J Biomed Mater Res 2001:2–I. https://doi.org/10.1002/1097-4636(200108)56:2<261::AID-JBM1094>3.0.C.O.

[20] Ding Y, Jiang Y, Xu F, Yin J, Ren H, Zhuo Q, et al. Preparation of nano-structured LiFePO4/graphene composites by co-precipitation method. Electrochem Commun 2010;12(1):10–3. https://doi.org/10.1016/j.elecom.2009.10.023.

[21] Julien CM, Mauger A, Zaghib K, Groult H. Comparative issues of cathode materials for Li-ion batteries. Inorganics 2014;2(1):132–54. https://doi.org/10.3390/inorganics2010132.

[22] Tang W, Hou Y, Wang F, Liu L, Wu Y, Zhu K. LiMn2O4 nanotube as cathode material of second-level charge capability for aqueous rechargeable batteries. Nano Lett 2013;13(5):2036–40. https://doi.org/10.1021/nl400199r.

[23] Tariq HA, Abraham JJ, Shakoor RA, Al-Qaradawi S, Karim MRA, Chaudhry U. Synthesis of lithium manganese oxide nanocomposites using microwave-assisted chemical precipitation technique and their performance evaluation in lithium-ion batteries. Energy Storage 2020;2(6). https://doi.org/10.1002/est2.202.

[24] Bao LY, Che HQ, Hu DZ, Su YF, Wang Z, Li N, et al. Methods for promoting electrochemical properties of LiNil/3Col/3Mnl/3O2 for lithium-ion batteries. Chin Sci Bull 2013;58(16):1869–75. https://doi.org/10.1007/s11434-013-5758-6.

[25] Yan H, Huang X, Chen L. Microwave synthesis of LiMn2O4 cathode material. J Power Sources 1999;81-82:647–50. https://doi.org/10.1016/S0378-7753(99)00112-3.

[26] Nakayama M, Watanabe K, Ikuta H, Uchimoto Y, Wakihara M. Grain size control of LiMn2O4 cathode material using microwave synthesis method. Solid State Ionics 2003;164(1–2):35–42. https://doi.org/10.1016/j.ssi.2003.08.048.

[27] Liu S, Yan P, Li H, Zhang X, Sun W. One-step microwave synthesis of micro/nanoscale LiFePO4/graphene cathode with high performance for lithium-ion batteries. Front Chem 2020;8. https://doi.org/10.3389/fchem.2020.00104.

[28] Dong Peng Z, Bing Cao Y, Rong Hu G, Du K, Guang Gao X, Wei Xiao Z. Microwave synthesis of Li2FeSiO4 cathode materials for lithium-ion batteries. Chin Chem Lett 2009;20(8):1000–4. https://doi.org/10.1016/j.cclet.2009.03.051.

[29] Fu YP, Su YH, Lin CH. Comparison of microwave-induced combustion and solid-state reaction for synthesis of LiMn2-xCrxO4 powders and their electrochemical properties. Solid State Ionics 2004;166(1–2):137–46. https://doi.org/10.1016/j.ssi.2003.09.018.

[30] Wei Y, Kim KB, Chen G. Evolution of the local structure and electrochemical properties of spinel LiNixMn2-xO4 ($0 \leq x \leq 0.5$). Electrochim Acta 2006;51(16):3365–73. https://doi.org/10.1016/j.electacta.2005.09.035.

[31] Chi LH, Dinh NN, Brutti S, Scrosati B. Synthesis, characterization and electrochemical properties of 4.8 V LiNi0.5Mn1.5O4 cathode material in lithium-ion batteries. Electrochim Acta 2010;55(18):5110–6. https://doi.org/10.1016/j.electacta.2010.04.003.

[32] Kebede MA, Yannopoulos SN, Sygellou L, Ozoemena KI. High-voltage LiNi 0.5 Mn 1.5 O 4- δ spinel material synthesized by microwave-assisted thermo-polymerization: some insights into the microwave-enhancing physico-chemistry. J Electrochem Soc 2017;164(13):A3259–65. https://doi.org/10.1149/2.1471713jes.

[33] James Abraham J, Nisar U, Monawwar H, Abdul Quddus A, Shakoor RA, Saleh MI, et al. Improved electrochemical performance of SiO2-coated Li-rich layered oxides-Li1.2Ni0.13Mn0.54Co0.13O2. J Mater Sci Mater Electron 2020;31(21):19475–86. https://doi.org/10.1007/s10854-020-04481-6.

[34] Ronduda H, Zybert M, Szczęsna A, Trzeciak T, Ostrowski A, Wieciński P, et al. Addition of yttrium oxide as an effective way to enhance the cycling stability of LiCoO2 cathode material for Li-ion batteries. Solid State Ionics 2020;335. https://doi.org/10.1016/j.ssi.2020.115426.

[35] Nisar U, Al-Hail SAJA, Petla RK, Shakoor RA, Essehli R, Kahraman R, et al. Understanding the origin of the ultrahigh rate performance of a SiO 2 -modified LiNi 0.5 Mn 1.5 O 4 cathode for lithium-ion batteries. ACS Appl Energy Mater 2019;2(10):7263–71. https://doi.org/10.1021/acsaem.9b01211.

[36] Shi Y, Chou SL, Wang JZ, Wexler D, Li HJ, Liu HK, et al. Graphene wrapped LiFePO 4/C composites as cathode materials for Li-ion batteries with enhanced rate capability. J Mater Chem 2012;22(32). https://doi.org/10.1039/c2jm32649c.

[37] Zhang H, Wang D, Shen C. In-situ EC-AFM and ex-situ XPS characterization to investigate the mechanism of SEI formation in highly concentrated aqueous electrolyte for Li-ion batteries. Appl Surf Sci 2020;507. https://doi.org/10.1016/j.apsusc.2019.145059.

[38] Rumberg B, Epding B, Stradtmann I, Kwade A. Identification of Li ion battery cell aging mechanisms by half-cell and full-cell open-circuit-voltage characteristic analysis. J Energy Storage 2019;25. https://doi.org/10.1016/j.est.2019.100890.

[39] Mohtat P, Nezampasandarbabi F, Mohan S, Siegel JB, Stefanopoulou AG. On identifying the aging mechanisms in li-ion batteries using two points measurements. Proc Am Control Conf 2017:98–103. https://doi.org/10.23919/ACC.2017.7962937.

[40] Akhoon SA, Sofi AH, Rubab S, Shah MA. Enhanced structural and electrochemical properties of LiMn2O4 nanocubes. J Electron Mater 2017;46(2):992–8. https://doi.org/10.1007/s11664-016-4741-9.

[41] Xue Y, Wang Z, Yu F, Zhang Y, Yin G. Ethanol-assisted hydrothermal synthesis of LiNi0.5Mn 1.5O4 with excellent long-term cyclability at high rate for lithium-ion batteries. J Mater Chem A 2014;2(12):4185–91. https://doi.org/10.1039/c3ta14567k.

[42] Raju K, Nkosi FP, Viswanathan E, Mathe MK, Damodaran K, Ozoemena KI. Microwave-enhanced electrochemical cycling performance of the LiNi0.2Mn1.8O4 spinel cathode material at elevated temperature. Phys Chem Chem Phys 2016;18(18):13074–83. https://doi.org/10.1039/c6cp01873d.

[43] Xu XL, Deng SX, Wang H, Liu JB, Yan H. Research progress in improving the cycling stability of high-voltage LiNi0.5Mn1.5O4 cathode in lithium-ion battery. Nano-Micro Lett 2017;9(2). https://doi.org/10.1007/s40820-016-0123-3.

[44] Capron O, Gopalakrishnan R, Jaguemont J, Van Den Bossche P, Omar N, Van Mierlo J. On the ageing of high energy lithium-ion batteries-comprehensive electrochemical diffusivity studies of harvested nickel manganese cobalt electrodes. Materials (Basel) 2018;11(2). https://doi.org/10.3390/ma11020176.

[45] Li J, He X, Zhao R, Wan C, Jiang C, Xia D, et al. Stannum doping of layered LiNi3/8Co2/8Mn3/8O2 cathode materials with high rate capability for Li-ion batteries. J Power Sources 2006;158(1):524–8. https://doi.org/10.1016/j.jpowsour.2005.08.026.

[46] Lee JW, Hwang D. Application of thermodynamic activity models to the equilibrium potential for lithium intercalation process of a cobalt-free cathode material with a layered structure. Comput Mater Sci 2015;100:80–3. https://doi.org/10.1016/j.commatsci.2014.09.006.

[47] Fang X, Ge M, Rong J, Zhou C. Graphene-oxide-coated LiNi0.5Mn1.5O4 as high voltage cathode for lithium ion batteries with high energy density and long cycle life. J Mater Chem A 2013;1(12). https://doi.org/10.1039/c3ta01534c.

[48] Kuenzel M, Kim G-T, Zarrabeitia M, Lin SD, Schuer AR, Geiger D, et al. Crystal engineering of TMPOx-coated LiNi0.5Mn1.5O4 cathodes for high-performance lithium-ion batteries. Mater Today 2020;39:127–36. https://doi.org/10.1016/j.mattod.2020.04.003.